Duc Quang VU[1*]

COMPARISON OF TUBE HYDROFORMING ABILITY WITH DIFFERENT PROTRUSION DIAMETERS OF HOLLOW T-JOINTS

This study investigates the formability of seamless copper hollow T-joints with varied protrusion-to-base diameter ratios manufactured through tube hydroforming (THF) using finite element analysis. Three configurations were simulated in Abaqus/CAE: T1 (protrusion diameter smaller than tube blank diameter), T2 (protrusion diameter equal to tube blank diameter), and T3 (protrusion diameter larger than tube blank diameter). Formability was comparatively assessed through four critical metrics: operational fluid pressure range enabling effective material flow for protrusion formation, plastic strain components, wall thickness distribution, and achievable protrusion height. The findings establish scientific and practical foundations for optimizing THF processes to manufacture high-integrity monolithic pipe connectors.

1. INTRODUCTION

Tube hydroforming (THF) leverages hydraulic fluid as a universal forming medium, enabling the production of complex hollow components through controlled pressure application [1–3]. This process mitigates localized stress concentrations by imposing uniform deformation pressures, thereby generating favorable stress-strain states essential for manufacturing high-integrity parts – including geometrically intricate configurations previously unattainable via conventional welding or casting [1, 2]. Tubular fittings constitute the predominant category of branched hollow components produced via THF [4, 5], with T-joints, X-connectors, reducers, and eccentric transitions representing common variants. Monolithic fittings fabricated through THF exhibit superior quality and accommodate diverse joining methods, including welding, threading, and brazing [6–8]. Process efficacy is significantly enhanced under combined loading conditions: simultaneous application of internal fluid pressure and axial compressive forces induces material plasticity [2, 8, 9], facilitating optimized material flow into deformation zones while maintaining advantageous stress triaxiality. The requisite fluid pressure is typically generated using specialized intensifier systems.

_____

[1] Department of Machines & Fundamentals of Machine Design, Faculty of Mechanical Engineering, University of Economics - Technology for Industries, Viet Nam
[*] E-mail: vuquang@uneti.edu.vn
  https://doi.org/10.36897/jme/214134

Recent advances in tube hydroforming (THF) control and simulation demonstrate significant progress in process optimization. Endelt [10] developed a simulation-tubulard feedback control framework for T-shaped aluminum alloy tubes (5049-O and 6060-T6) with constant-diameter protrusion, enhancing product stability while shortening operational procedures. Xu [11] optimized THF loading paths for 5A02 aluminum tubes (45–55 mm diameter expansion) by integrating FEM (Abaqus/CAE) with genetic algorithm-tuned fuzzy membership functions, effectively minimizing uneven deformation. Further enhancing computational efficiency, Cheng [12] combined FEM with Random Forest machine learning for real-time CP-Ti titanium tube hydroforming simulations, maintaining high accuracy in defect prediction. Geometric parameter studies by Trung [13] identified protrusion inclination angles as critical for hollow joint formability, thickness distribution, and structural integrity. Karami [14] quantitatively validated through XRD measurements that T-shaped steel tubes exhibit severe residual stresses and thickness reduction (~24%) at transition zones, mitigated by pressure/axial force optimization. For formability prediction, Yuenyong [15] demonstrated the superiority of GISSMO damage mechanics models over traditional FLD in forecasting SUS304 stainless steel failure locations. Trinh [16, 17] addressed complex geometries via multi-stage hydroforming: cross-shaped carbon steel components required independent pressure control at four junctions, while U-shaped branched parts benefited from 45° branch angles and differential pressure zoning. Complementing these, Abdullah [18] achieved > 95% spring back prediction accuracy in sheet/tube forming using enhanced FEM with Chaboche kinematic hardening and shell theory, identifying holding pressure as a critical suppression factor. Three-dimensional simulation constitutes an indispensable tool in modern metal forming, offering critical advantages including development cost reduction, early defect prediction, material optimization, complex process modelling, and enhanced product quality [19–21]. This study employs Abaqus/CAE software – a general-purpose nonlinear FEA software suitable for simulating the hydroforming process of forming three seamless copper T-joint configurations with varying branch-to-tubular diameter ratios: *T1* (protrusion diameter $Dp = 19.05$ mm < seamless tube blank diameter $D0 = 22.22$ mm), *T2* ($Dp = D0$), and *T3* ($Dp = 25.04$ mm > $D0$) [21]. Formability assessment encompasses four critical parameters: operational fluid pressure range enabling effective material flow for protrusion formation, plastic strain components (PE), wall thickness distribution (STH), and achievable protrusion height (U1). Another novelty is the study and recognition of the parallel forming of three different product diameters from the same pipe batch and the use of the FEM method to determine practical relationships for optimizing the parameters (internal pressure of the working fluid, axial feed, batch geometry) for the production of these copper T-joints.

2. MATERIALS AND METHODS

2.1. TUBULAR BLANK AND MATERIAL PROPERTIES OF THE TUBULAR BLANK

The geometric model, mesh discretization, and material model of the tubular blank, configured uniformly for all three forming processes of parts T1, T2, and T3 in Abaqus/CAE software, are detailed in Table 1 and Table 2.

Table 1. The tubular blank was utilized for both the geometric modelling and mesh generation
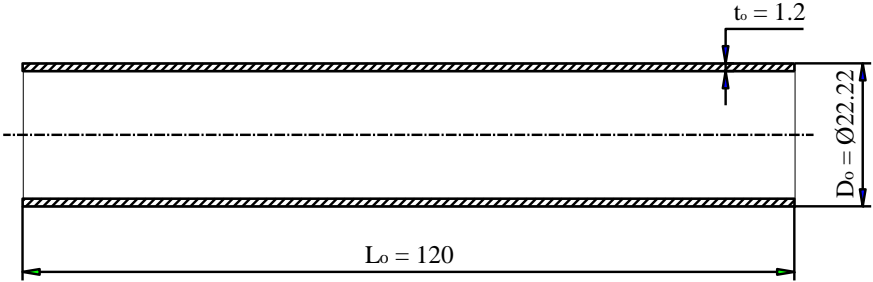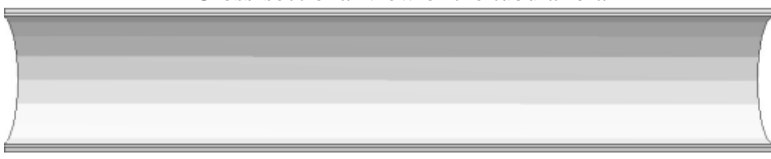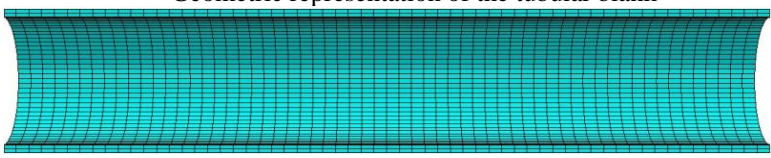
Parameters	Symbol/unit	Value
$t_o = 1.2$ ... $L_o = 120$ ... $D_o = \varnothing 22.22$ Cross-sectional view of the tubular blank		
Geometric representation of the tubular blank		
Finite element mesh model of the tubular blank Identical Create Part configurations were applied to the tubular blank for all three forming processes (*T1*, *T2*, *T3*): Modelling Space: 3D, Type: Deformable, Tubular Feature: Shell, Mesh Configuration: Element count: 2340, Element shape: Quad, Technique: Free, Algorithm: Medial axis.		
Outside diameter	D_0 (mm)	22.22
Inside diameter	d_I (mm)	19.82
Initial thickness	t_0 (mm)	1.2
Initial length	L_0 (mm)	120

Table 2. The material properties of the copper tubular blank implemented in the material model

Material properties of the copper tubular blank	Value
Temperature (ºC)	24
Density, ρ (kg/m^3)	8940
Young's modulus, E (GPa)	115
Hardening coefficient, K (MPa)	325
Work hardening exponent, n	0.54
Poisson's ratio, v	0.33
Yield strength, σ_Y (MPa)	57.08
Ultimate tensile strength, σ_U (MPa)	231.09
Elongation (%)	42.75

2.2. FORMING DIE MODELS

The core dimensions of all three die cavities include: length 130 mm, width 110 mm, thickness 25 mm. The blank-holding cavity diameter equals the tubular blank's outer

diameter. The forming cavities for *T1*, *T2*, and *T3* hollow joints - detailed in table 3 - were geometrically modelled and assembled into a simulation module comprising four components: a rigid die, left rigid punch, right rigid punch, and a tube blank (Fig. 1).

Table 3. The geometric parameters of the three forming dies employed in the numerical model

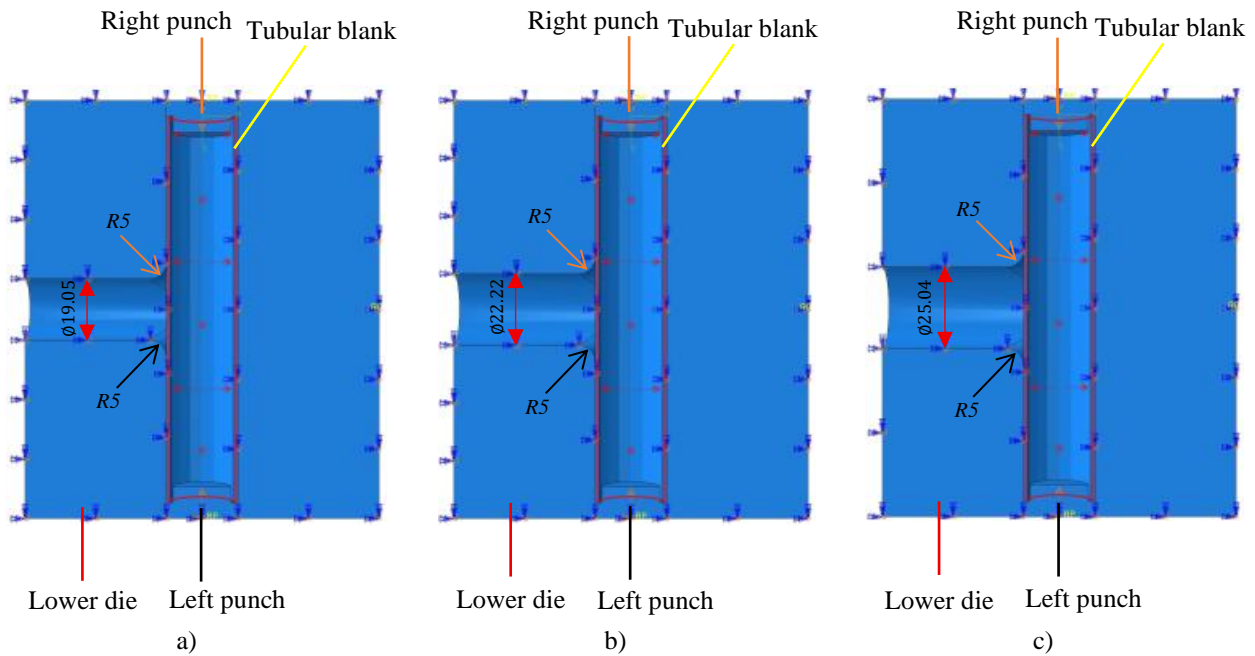| Hollow T-Joints	Dimensions of the die cavity used for protrusion D_p (mm)	Tool filling radius
		Leftward fillet radius = Rightward fillet radius = R_f (mm)
T1	$D_p = 19.05$ (mm) $< D_0$	$R_f = 5$ (mm) $\geq 4t_0 = 4.8$ (mm)
T2	$D_p = 22.22$ (mm) $= D_0$	$R_f = 5$ (mm) $\geq 4t_0 = 4.8$ (mm)
T3	$D_p = 25.04$ (mm) $> D_0$	$R_f = 5$ (mm) $\geq 4t_0 = 4.8$ (mm)

Fig. 1. The assembly of the tubular blank and dies for forming hollow T-joints: a) *T1*, b) *T2*, c) *T3*

2.3. COMPUTATION AND IMPLEMENTATION OF BOUNDARY CONDITIONS

To prevent wrinkling during tube hydroforming of *T*-shaped joints, Bogojavlenski and Serjakow [2] developed an empirical correlation for determining the minimum internal pressure (Pmin), independent of counter punch force and tube blank length, as expressed in equation (1):

$$P_{min} = \left(0.13 + 1.15\frac{t_0}{D_p}\right)\sigma_Y \tag{1}$$

The bursting pressure (P_b) represents the maximum pressure enabling tube expansion without rupture. For *T*-shaped hydroforming without counter punches, P_b can be estimated using equation (2) [22]. This formulation derives from the balanced biaxial protrusion

phenomenon in metal sheets, justified by the (approximate) dominant balanced biaxial tensile state at the protrusion apex when counter punches are absent.

$$P_b = \sigma_U \left(\frac{4t_0}{D_p - t_0} \right) \qquad (2)$$

Using $\sigma_Y = 57$ MPa, $\sigma_U = 231.09$ MPa, $t_0 = 1.2$ mm, $D_0 = 22.22$ mm, and $D_p = 19.05$, 22.22, 25.04 mm (Tables 1–3), equations (1) and (2) yield: $P_{min\text{-}T1} = 7.96$ MPa, $P_{b\text{-}T1} = 62.14$ MPa; $P_{min\text{-}T2} = 7.88$ MPa, $P_{b\text{-}T2} = 52.77$ MPa; $P_{min\text{-}T3} = 7.83$ MPa, $P_{b\text{-}T3} = 46.61$ MPa. These values establish initial benchmarks for simulating the hydroforming process, where working fluid pressure (P_i (MPa)) and axial feed (Af (mm)) are simultaneously applied from both tube ends. Pi-max follows a 20-second forming cycle loading path - Amp-1 (Fig. 2), while axial feed Af = 30 mm adheres to another 20-second cycle - Amp-2 (Fig. 3). A friction coefficient of 0.1 was assigned between the tube and die surfaces [2]. Identical boundary conditions were implemented in Abaqus/CAE for all three simulations to comparatively analyse the formability of hollow joints *T1*, *T2*, and *T3*.

Edit Amplitude		×
Name: Amp-1		
Type: Tabular		
Time span: Step time		
Smoothing: ● Use solver default		
○ Specify:		
Amplitude Data Baseline Correction		

	Time/Frequency	**Amplitude**
1	0	0
2	0.5	1
3	1	1

Edit Amplitude		×
Name: Amp-2		
Type: Tabular		
Time span: Step time		
Smoothing: ● Use solver default		
○ Specify:		
Amplitude Data Baseline Correction		

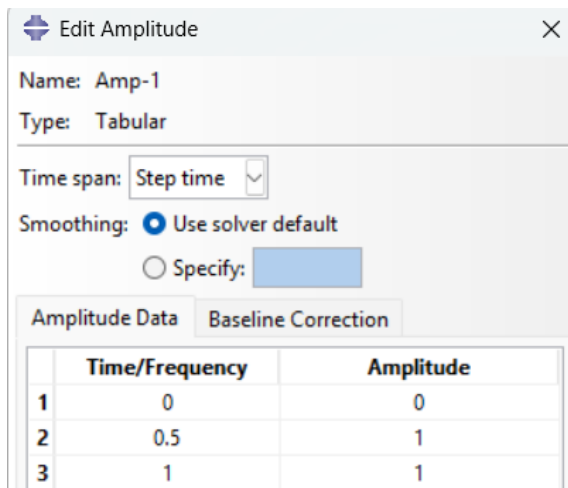|	**Time/Frequency**	**Amplitude**
1	0	0
2	0.5	0.5
3	1	1

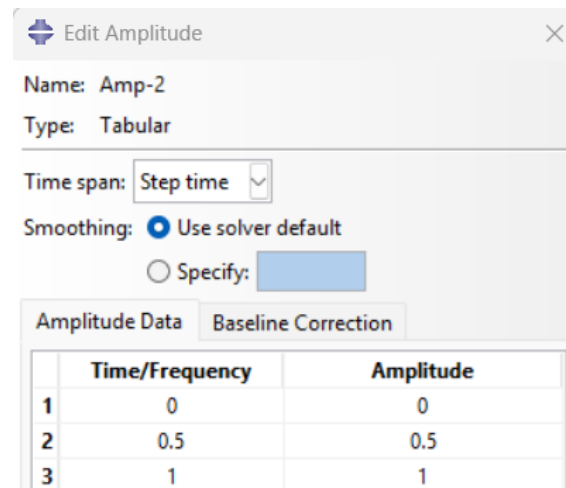Fig. 2. Fluid pressure (P_i (MPa)) loading path for a 20-second forming cycle

Fig. 3. Axial feed (Af (mm)) loading path for a 20-second forming cycle

3. RESULTS AND DISCUSSION

Tubular on fluid pressure domains, axial feed data, and simulation results for hydroforming processes of *T1, T2*, and *T3* joints, the author conducted comparative analysis across four input/output criteria, detailed below.

3.1. FLUID PRESSURE DOMAIN FOR EFFECTIVE MATERIAL FLOW DURING PROTRUSION FORMATION

Using the Amp-1 fluid pressure loading path ($P_{i\text{-}max} = 20$ MPa) and Amp-2 axial feed path ($Af = 30$ mm per tube end) during protrusion forming of T-joints yielded the results in

Fig. 4. Forming stresses reached $S_{max} = 231.09$ MPa in both the guide region (subjected to compressive axial stress *S33*) and transition zone (experiencing high shear stress *S12* from bending+friction), where simultaneous axial compression and fluid pressure drove material flow along die contours. These peak stresses posed no failure risk due to continuous tube-die contact, which enhanced part stiffness through strain hardening - a key advantage of tube hydroforming. The protrusion cavity region (Fig. 4) shows plastic deformation under fluid pressure, drawing material into the expanded joint section. The protrusion apex experienced dominant biaxial stresses (*S11, S22*), with rupture risk if exceeding $\sigma_U = 231.09$ MPa (recommended: von Mises stress < 90% σ_U). All three joints maintained safe forming stresses with complete die filling at the protrusion walls. Protrusion height conformity followed: *T1* exhibited the lowest conformity (Fig. 4a), followed by *T2* (Fig. 4b), with *T3* achieving the highest (Fig. 4c). Since effective protrusion heights fell below design targets at $P_{i-max} = 20$ MPa, additional simulations with elevated pressure were performed to determine the effective material flow pressure domain (Fig. 5).
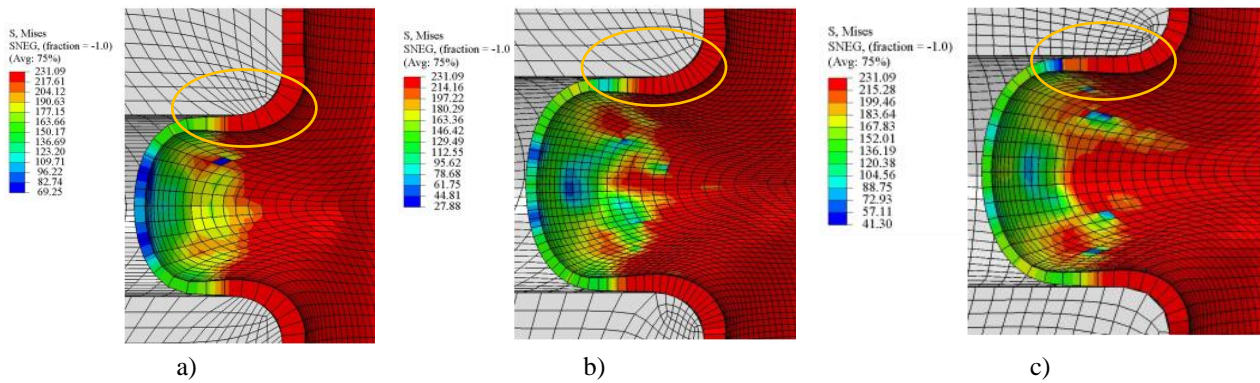

Fig. 4. Von Mises stress distribution (MPa) and material flow during protrusion forming at $P_{i-max} = 20$ MPa, $Af = 30$ mm: (a) *T1*, (b) *T2*, (c) *T3*

Figure 5a, b, and c establishes the effective fluid pressure domains for *T1-T3* joints under identical Amp-1/Amp-2 loading paths. Smaller-diameter protrusions (*T1*) required higher pressures (30 ÷ 40 MPa), same-diameter protrusions (*T2*) needed moderate pressures (25 ÷ 35 MPa), while larger-diameter protrusions (*T3*) used lower pressures (23 ÷ 30 MPa). Three output parameters were subsequently compared tubulard on these domains.

Exceeding the effective pressure domain caused unsafe thinning (STH$_{min}$ < 0.84 mm corresponds to $\varepsilon_{min} < -30\%$) and protrusion rupture. Failure occurred at: $P_{i-max} = 45$ MPa for *T1* (Fig. 6a), 40 MPa for *T2* (Fig. 6b), and 35 MPa for *T3* (Fig. 6c). Fig. 6 documents the critical fluid pressure limit Pi-max under Amp-1 loading path that causes rupture at the protrusion apex - a failure mechanism predominant in expansion zones due to excessive biaxial stretching. The identified pressure domains (Fig. 5) demonstrate an inverse relationship between protrusion diameter and required pressure: smaller protrusions (*T1*) necessitated 30 ÷ 40 MPa pressures, while larger protrusions (*T3*) achieved forming at 23 ÷ 30 MPa. Exceeding these domains induced critical thinning ($\varepsilon_{min} < -30\%$) and rupture at the protrusion apex (Fig. 6), confirming that strain localization accelerates failure when von Mises stress approaches 90% of σ_U.
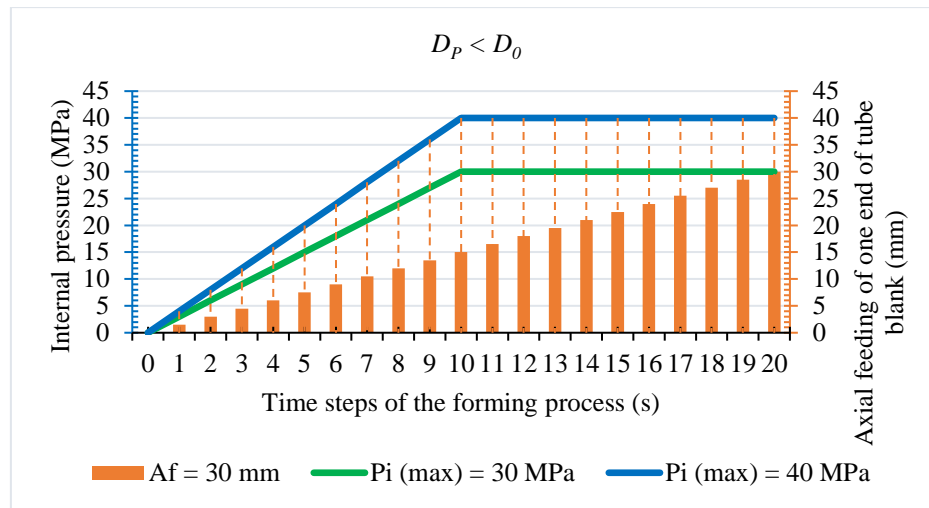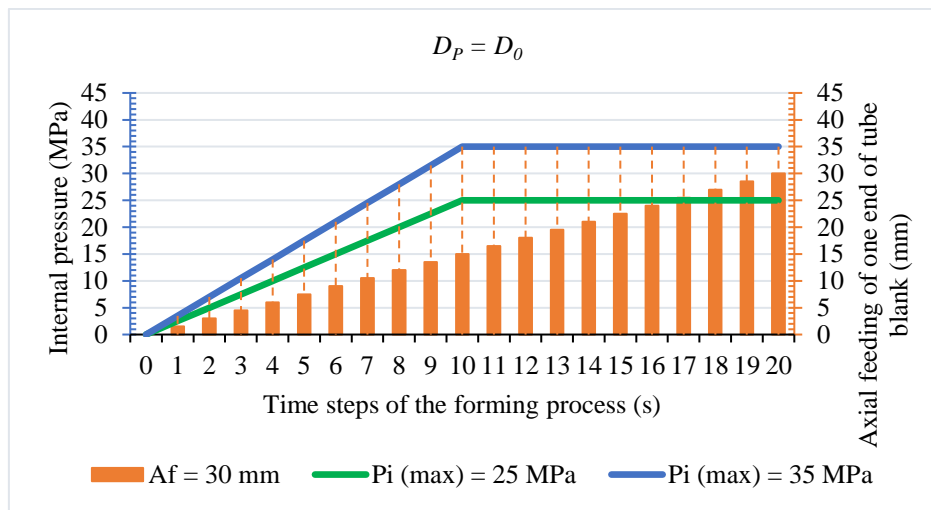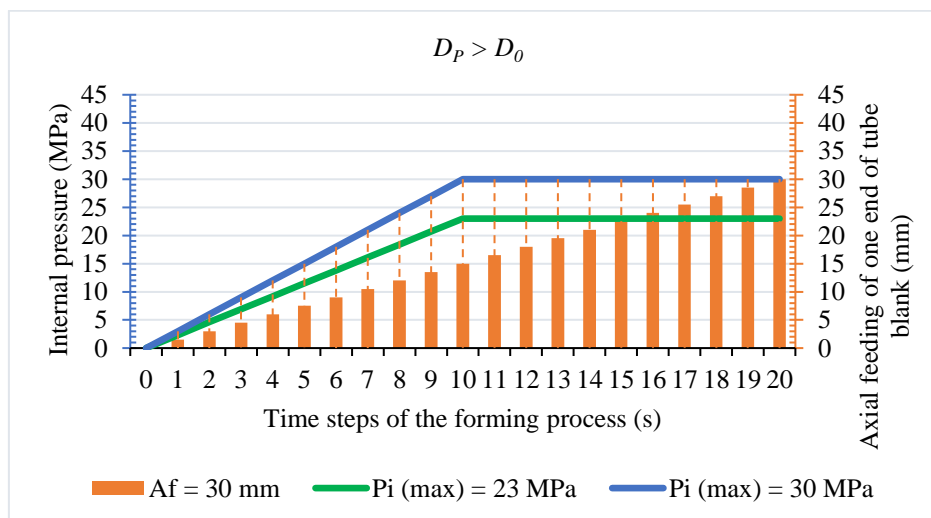
Fig. 5. Effective fluid pressure domain for protrusion forming material flow: a) *T1*, b) *T2*, c) *T3*
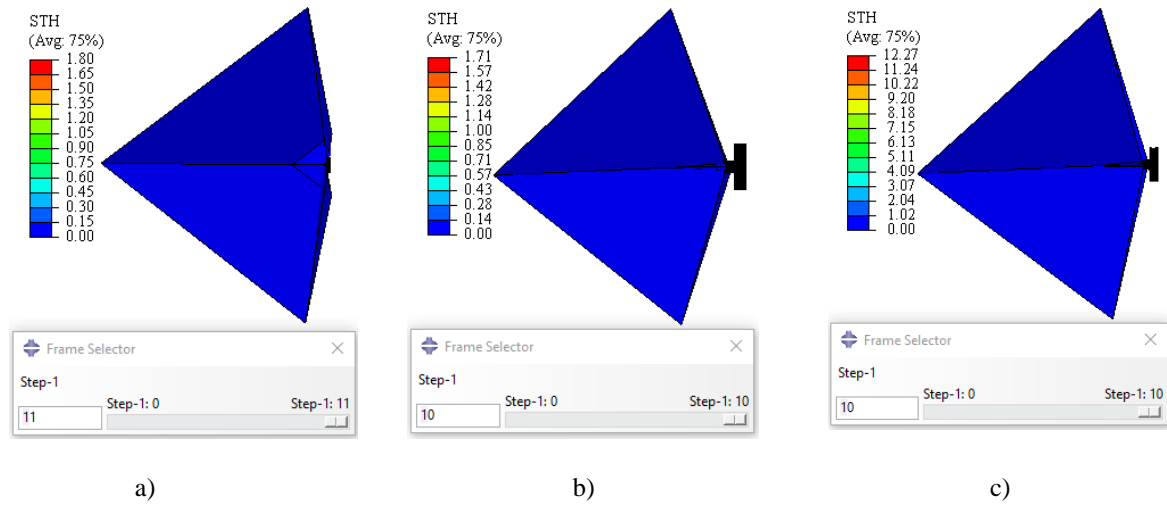
Fig. .6. Critical fluid pressure limit $P_{i\text{-}max}$ (under Amp-1 loading path) causing rupture at the protrusion apex ($STH_{min} <$ 0.84 mm) during the forming process: a) *T1 ($P_{i\text{-}max}$ = 40 MPa)*, b) *T2 ($P_{i\text{-}max}$ = 35 MPa)*, c) *T3 ($P_{i\text{-}max}$ = 30 MPa)*

3.2. PLASTIC STRAIN COMPONENTS IN THE HOLLOW T-JOINTS

The plastic strain (*PE*) components of *T1 ($P_{i\text{-}max}$ = 40 MPa)*, *T2 ($P_{i\text{-}max}$ = 35 MPa)*, and *T3 ($P_{i\text{-}max}$ = 30 MPa)* joints - formed at the upper limits of their effective material flow pressure domains (Figs. 7a-c) - elucidate the material's nonlinear deformation behaviour. Guide regions at both tube ends exhibited compressive strains $PE_{min\text{-}T1}$ = -0.22 ≈ $PE_{min\text{-}T2}$ = -0.23 ≈ $PE_{min\text{-}T3}$ = -0.21 due to axial compressive stress (*S33*) facilitating material supplementation. Transition zones displayed both tensile (positive) and compressive (negative) strain components (Fig. 7), with peak values occurring in high-shear regions (*S12*) from bending+friction. Maximum strains (red zones on the scale) initiated at the expansion center and propagated toward the protrusion, registering $PE_{max\text{-}T1}$ = 0.94 (Fig. 7a), $PE_{max\text{-}T2}$ = 0.92 (Fig. 7b), and $PE_{max\text{-}T2}$ = 0.93 (Fig. 7c) - all within safe plastic deformation limits. Expansion regions showed moderate positive strains (0.16 ÷ 0.55) under dominant biaxial stress (*S11*, *S22*), confirming safe formability for copper material.
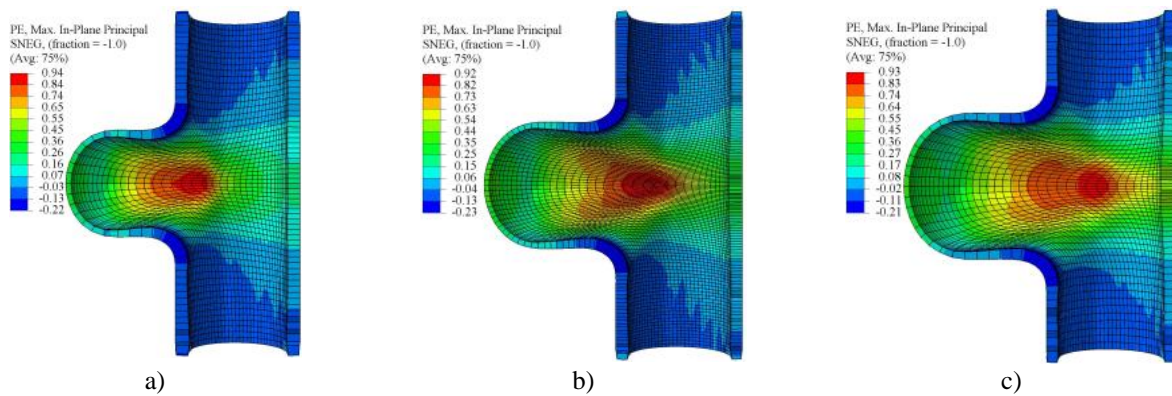

Fig. 7. Distribution of plastic strain components in the hollow T-joints: a) *T1 ($P_{i\text{-}max}$ = 40 MPa)*, b) *T2 ($P_{i\text{-}max}$ = 35 MPa)*, c) *T3 ($P_{i\text{-}max}$ = 30 MPa)*

Figure 8 illustrates peak plastic strains (PE_{max}) versus fluid pressure within optimized forming domains. PE_{max} increased with pressure for all joints. At 30 MPa: $PE_{max-T1} = 0.87 < PE_{max-T2} = 0.89 < PE_{max-T3} = 0.93$, indicating significant strain variation between small and large protrusions. At 35 MPa: $PE_{max-T1} = 0.91 \approx PE_{max-T2} = 0.92$ demonstrated comparable strain values. At 25 MPa: $PE_{max-T2} = 0.85 < PE_{max-T3} = 0.9$ revealed substantial strain divergence when forming same-diameter versus larger-diameter protrusions.
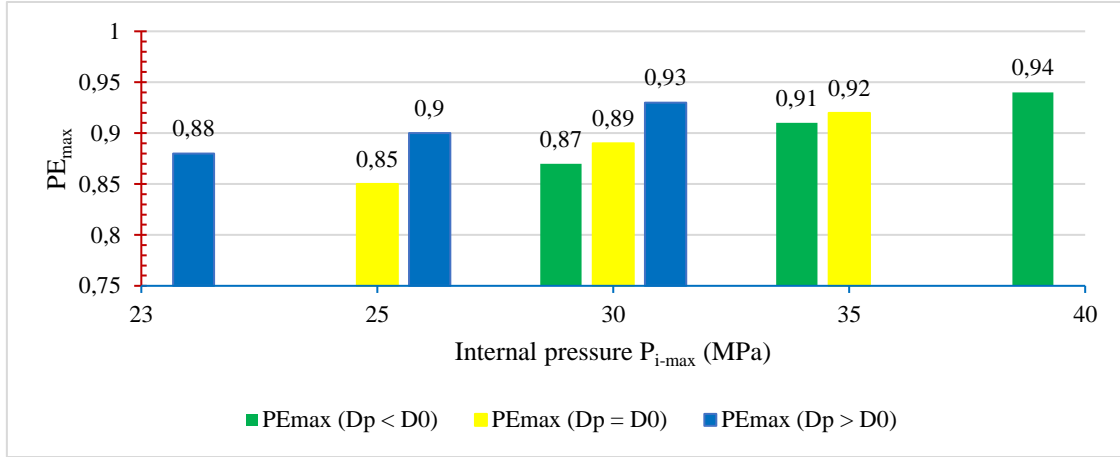

Fig. 8. Plastic strain components in hollow T-joints under optimized material flow pressure domains: a) *T1 ($P_{i-max} = 30$, 35, 40 MPa)*, b) *T2 ($P_{i-max} = 25$, 30, 35 MPa)*, c) *T3 ($P_{i-max} = 23$, 25, 30 MPa)*

3.3. TUBE WALL THICKNESS DISTRIBUTION IN THE HOLLOW T-JOINTS

Figure 9 illustrates wall thickness distribution (*STH (mm)*) in *T1* ($P_{i-max} = 40$ MPa), *T2* ($P_{i-max} = 35$ MPa), and *T3* ($P_{i-max} = 30$ MPa) hollow joints. *STH* nonuniformity across three zones results from differential stress-strain states during forming, with thinning concentrated at protrusion apex regions. All joints satisfied copper's maximum allowable thinning ($\varepsilon_{min} = -30\%$, equivalent to $STH_{min} = 0.84$ mm).
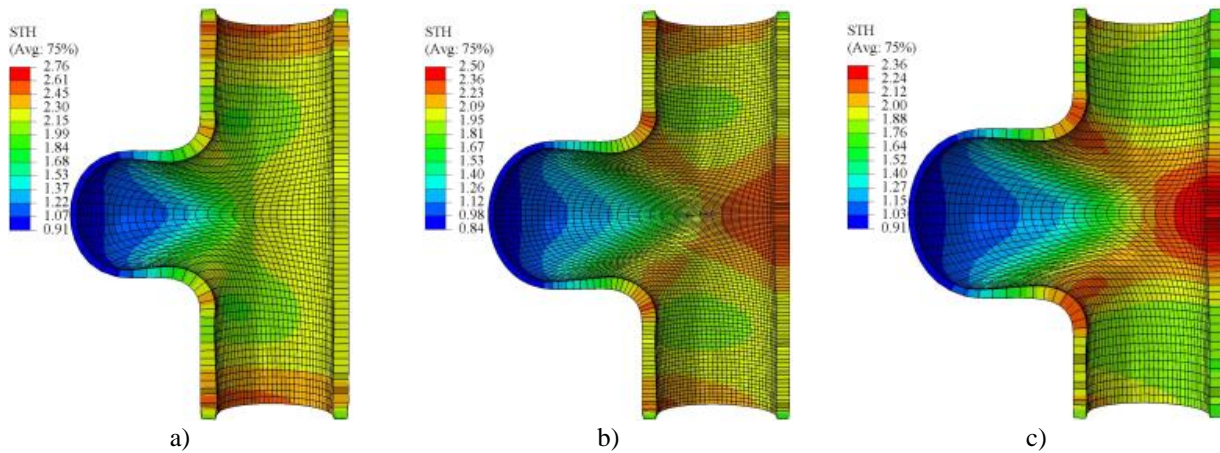

Fig. 9. Tube wall thickness distribution in the hollow T-joints (STH (mm)): a) *T1 ($P_{i-max} = 40$ MPa)*, b) *T2 ($P_{i-max} = 35$ MPa)*, c) *T3 ($P_{i-max} = 30$ MPa)*

Conversely, guide and transition zones exhibited thickening: STH_{max-T1} = 2.76 mm (130% thickening), STH_{max-T2} = 2.50 mm (108%), and STH_{max-T3} = 2.36 mm (97%), causing internal wrinkling. Specific distributions include: *T1*: Peak thickness (STH_{max-T1} = 2.76 mm) at guide zone ends; balanced wall thickness (STH = 2.15 ÷ 2.30 mm) opposite protrusion; apex thinning to STH_{min-T1} = 0.91 mm (ε_{min-T1} = -24.2%) (Fig. 9a). *T2*: Maximum thickness (STH_{max-T2} = 2.50 mm) mid-section opposite protrusion; uniform distribution (STH = 1.95 ÷ 2.50 mm); apex thinned to STH_{min-T2} = 0.84 mm (ε_{min-T2} = -30%) (Fig. 9b). *T3*: Thickening (STH_{max-T3} = 2.36 mm) mid-section opposite protrusion; STH range 1.52 ÷ 2.36 mm; apex thinning matching T1 (STH_{min-T3} = 0.91 mm, ε_{min-T3} = -24.2%) (Fig. 9c).

Figure 10 compares STH_{min} at protrusion apex across joints under optimized pressures versus initial thickness t_0. STH_{min} decreased with increasing P_{i-max}, most severely in *T2* (t_0 = 1.2 mm → 1.04 → 0.97 → 0.84 mm), followed by *T1* (t_0 = 1.2 → 1.04 → 0.98 → 0.91 mm), and least in *T3* (t_0 = 1.2 → 1.04 → 1.01 → 0.91 mm). However, the critically thinned area (blue zones) expanded progressively from *T1* to *T3* (Fig. 9). Controlled thinning within safety limits maximized achievable protrusion height ($U1_{max}$) and effective protrusion formation.

Controlled thinning at protrusion apexes (Fig. 9) remained within copper's forming limit ($\varepsilon_{min} = -30\%$), with safety margins highest in larger-diameter joints (*T3*: $\varepsilon_{min-T3} = -24.2\%$ at 30 MPa). The inverse thickness-diameter relationship - evidenced by *T1*'s 0.91 mm minimum thickness versus *T2*'s 0.84 mm at comparable pressures - underscores diameter-dependent strain sensitivity in small expansions (Fig. 10).
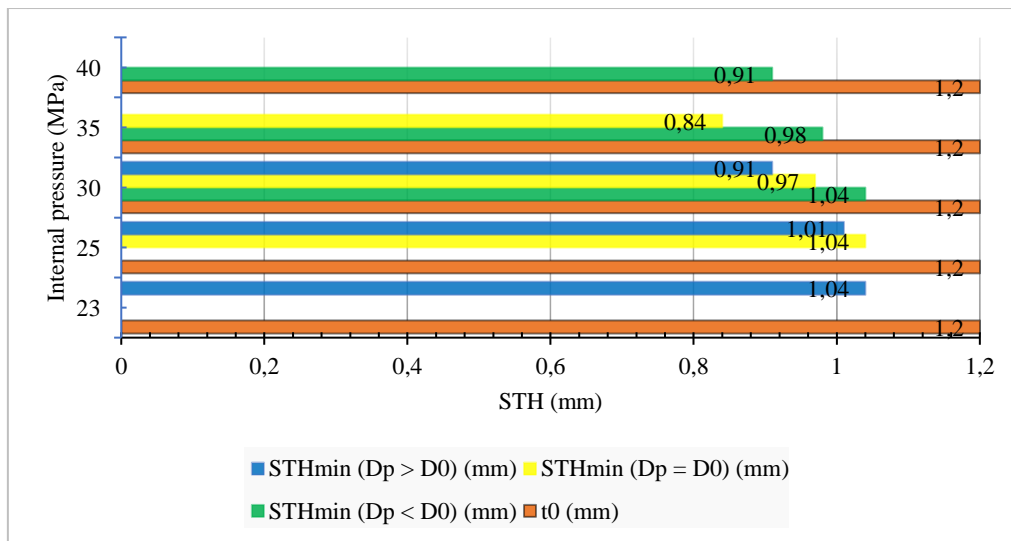

Fig. 10. STH_{min} in the hollow T-joints: a) *T1 (P_{i-max} = 30, 35, 40 MPa)*, b) *T2 (P_{i-max} = 25, 30, 35 MPa)*, c) *T3 (P_{i-max} =23, 25, 30 MPa)*

3.4. HEIGHT OF THE SHAPED PROTRUSIONS IN THE HOLLOW T-JOINTS

The measured protrusion heights *U1 (mm)* for *T1 (P_{i-max} = 40 MPa)*, *T2 (P_{i-max} = 35 MPa)*, and *T3 (P_{i-max} = 30 MPa)* joints were $|U1_{T1}|$ = 19.65 mm (Fig. 11a), $|U1_{T2}|$ = 23.33 mm (Fig. 11b), and $|U1_{T3}|$ = 24.89 mm (Fig. 11c) respectively. The resulting protrusion-to-blank

diameter ratios were: $U1_{T1} / D_0 = 0.88$ (lowest), $U1_{T2} / D_0 = 1.05$, and $U1_{T3} / D_0 = 1.12$ (highest). This demonstrates that larger protrusion-to-initial diameter ratios (D_p / D_0) correlate with increased protrusion height $U1$, consequently enhancing effective protrusion formation.
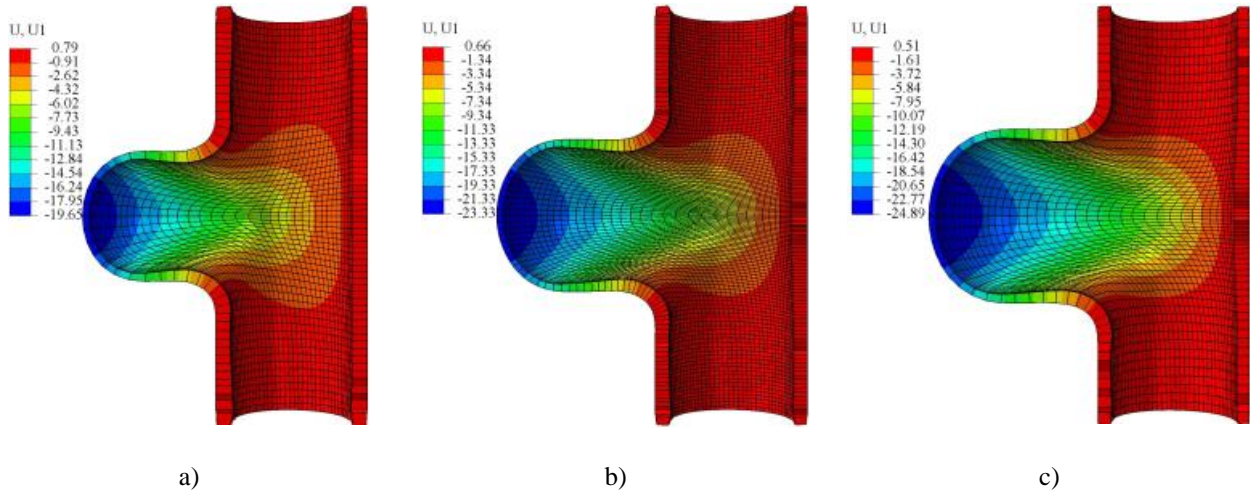

Fig. 11. Height of the shaped protrusion (U1 (mm)) in the hollow T-joints: a) *T1 ($P_{i-max} = 40$ MPa)*, b) *T2 ($P_{i-max} = 35$ MPa)*, c) *T3 ($P_{i-max} = 30$ MPa)*

As illustrated in Fig. 12, a clear and consistent positive correlation was observed between the maximum internal pressure (P_{i-max}) and the protrusion height ($U1$) for all three T-joints (*T1, T2, T3*) under a constant total axial feed (Af_{Σ}) of 60 mm. This trend underscores the fundamental role of internal pressure as the primary driving force for material deformation into the die cavity. The quantitative data reveals this relationship: for *T1*, *U1* increased from 17.47 mm to 19.65 mm as P_{i-max} rose from 30 MPa to 40 MPa; for *T2*, it grew from 19.88 mm to 23.33 mm with P_{i-max} increasing from 25 MPa to 35 MPa; and for *T3*, *U1* rose from 21.96 mm to 24.89 mm corresponding to a P_{i-max} increase from 23 MPa to 30 MPa.
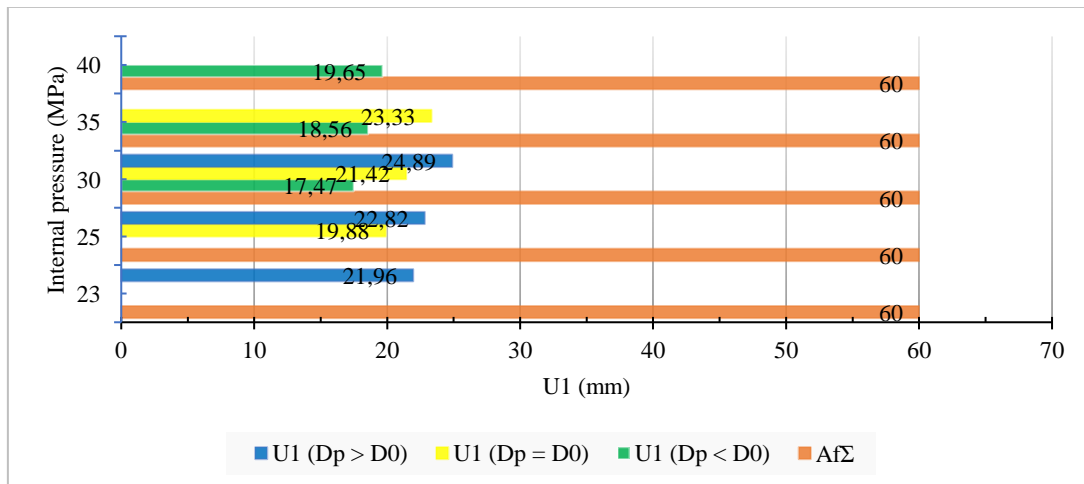

Fig. 12. Comparative protrusion height analysis under optimized material flow pressure domains: a) *T1 ($P_{i-max} = 30, 35, 40$ MPa)*, b) *T2 ($P_{i-max} = 25, 30, 35$ MPa)*, c) *T3 ($P_{i-max} = 23, 25, 30$ MPa)*

Notably, the baseline and sensitivity of the joints to pressure vary significantly. *T3* achieved the highest protrusion height (24.89 mm) at a relatively lower pressure (30 MPa), whereas *T1* required a much higher pressure (40 MPa) to reach a notably lower height (19.65 mm). This key observation suggests that the geometry and/or material conditions of *T3* are more conducive to efficient forming, requiring less pressure to achieve greater deformation. Furthermore, the progression of data points indicates that the rate of increase in *U1* per unit of $P_{i\text{-}max}$ might not be linear and could differ between joints, a nuance that warrants further investigation for process optimization.

4. CONCLUSION

This study analysed and compared four input/output parameters for successfully hydroforming three hollow T-joints (T1, T2, T3) with distinct protrusion diameters through numerical simulations in Abaqus/CAE. The optimized parameters for each joint provide foundational data for die design/manufacturing and process configuration, enabling subsequent experimental validation and scalable fabricating of diverse T-shaped tubular connectors.

Diameter-Thinning Relationship: Constant-diameter joints (T2) exhibit higher thinning (ε_{min} = -30%) than expanded/reduced diameters (T1, T3: -24.2%), indicating greater formability limits for diameter-changing geometries.

Pressure-Diameter Interdependence: Smaller protrusion (T1: Dp /D0 = 0.86) require 30 ÷ 40 MPa pressures - approximately 40% higher than larger expansions (*T3*: Dp /D0 = 1.13 at 23 ÷ 30 MPa), demonstrating that pressure requirements decrease as expansion ratio increases.

Strain-Height Tradeoff: Despite similar PEmax values (0.92 ÷ 0.94), *T2* achieved 19% greater protrusion height than *T1* at 35 MPa versus 40 MPa, revealing that strain distribution efficiency outweighs peak strain magnitude in height optimization.

REFERENCES

[1]   PHAM N.V., 2006, *Hydraulic Stamping Technology*, Hanoi University of Science and Technology.
[2]   KOÇ M., 2008, *Hydroforming for Advanced Manufacturing, 1st ed*, Woodhead Publishing Limited, Cambridge England.
[3]   ALASWAD A., et al., 2012, *Tube Hydroforming Process: a Reference Guide*, Materials and Design, 33, 328–339.
[4]   REDDY P.V., et al., 2020, *Evolution of Hydroforming Technologies and Its Applications – a Review*, J. Adv. Manuf. Syst., 19, 737-780.
[5]   BELL C., et al., 2020, *A State of the Art Review of Hydroforming Technology: its Applications, Research Areas, History, and Future in Manufacturing*, Int. J Mater. Form., 13,.789–828.
[6]   CHINCHANIKAR S., et al., 2024, *A Review of Emerging Hydroforming Technologies: Design Considerations, Parametric Studies, and Recent Innovations*, J. Eng. Appl. Sci., 71, 205.
[7]   NIELSEN C.V., MARTINS P.A.F., 2021, *Metal Forming: Formability*, Simulation, and Tool Design, 1st ed. London, England: Academic Press – Elsevier Inc.
[8]   SCHULER G., 1998, *Metal Forming Handbook*, 1st ed. Berlin, Germany: Springer.

[9] HWANG YM., et al., 2025, *Performance Evaluation and Loading Path Design in Tube Hydroforming of Multi-Convolution Metal Bellows*, Int. J. Adv. Manuf. Technol., https://doi.org/10.1007/s00170-025-16611-7.

[10] ENDELT B., 2022, *In Process Feedback Control of Tube Hydro Forming Process*, The International Journal of Advanced Manufacturing Technology, 119, 7723–7733.

[11] XU Y., et al., 2024, *Fuzzy Control Optimization of Loading Paths for Hydroforming of Variable Diameter Tubes*, Computers, Materials & Continua, 81/2, 2753-2768.

[12] CHENG L., et al., 2024, *Real-Time Simulation of Tube Hydroforming by Integrating Finite-Element Method and Machine Learning*, Journal of Manufacturing and Materials Processing, 8/4, 175.

[13] TRUNG N.D., et al., 2025, *The Influence of the Protrusion Inclination Angle on the Formability of Hollow Joint in the Tube Hydroforming Process*, Journal of Machine Engineering, 25/3, 5–18, https://doi.org/10.36897/jme/203468.

[14] KARAM, J.S., et al., 2019, *Numerical and Experimental Study of Residual Stress Measurement and Thickness Distribution of T-Shape Steel Tube Produced by Tube Hydroforming*, Journal of Modern Processes in Manufacturing and Production, 8/1, 45–58.

[15] YUENYONG J., et al., 2017, *Formability Prediction for Tube Hydroforming of Stainless Steel 304 Using Damage Mechanics Model*, Journal of Manufacturing Science and Engineering, 140/1, 011006.

[16] TRINH M.T., et al., 2025, *Hydro-Forming a Cross-Shaped Component from Tube Billet*, Journal of Machine Engineering, 25/2, 111-122, https://doi.org/10.36897/jme/204661.

[17] TRINH M.T., et al., 2025, *Hydro-Forming of U-Shaped Parts with Branches, Engineering*, Technology & Applied Science Research. Greece, 15/1, 19226–19231.

[18] ABDULLAH E., et al., 2025, *Enhancing Experimental Prediction of Springback in Forming Processes Using Advanced Finite Element Modelling*, Journal of Machine Engineering, 25/1, 79–101, https://doi.org/10.36897/jme/202916.

[19] VU Q.D., 2024, *Effect of Contact Blast Loading on the Plastic Deformation Forming Ability of Large Steel Pipes*, EUREKA: Physics and Engineering, 4, 124–132.

[20] QUANG V.D., 2025, *The Optimization of Rotary Bending Die Process: Criteria for the Metal Sheet Angles and Springback Effects*, Eng. Technol. Appl. Sci. Res., 15/1, 20553–20558.

[21] Abaqus/Explicit 3DEXPERIENCE R2017X, Dassault Systemes SIMULIA Corp. 1301 Atwood Avenue, Suite 101W Jonhston, RI 02919, USA.

[22] JIRATHEARANAT S.., et al., 2000, *Evaluation of Metal Flow in Tube Hydroforming of Y-Shapes*, Progress Report - FE Simulations, ERC/NSM report, THF/ERC/NSM-99-R-41a.